Progress in Reaction Kinetics and Mechanism

ARTICLE

Open Access

https://doi.org/10.48130/prkm-0025-0006

Progress in Reaction Kinetics and Mechanism **2025**, 50: e006

Kinetic and thermodynamic evaluation of adsorptive removal of lead(II) from aqueous solutions using Polypyrrole@$CoFe_2O_4$ nano-adsorbent

Abhishek Srivastava[1*], Neetu Srivastava[2], Rashmi Nayak[3] and Ruchi Singh[4]

[1] *Department of Chemistry, GLA University, Mathura, U.P., India*
[2] *Department of Chemistry, D.D.U. Gorakhpur University, Gorakhpur, U.P., India*
[3] *Department of Botany, D.D.U. Gorakhpur University, Gorakhpur, U.P., India*
[4] *Department of Chemistry, B. N College of Engineering & Technology, Lucknow, U.P., India*
* Corresponding author, E-mail: aabhichem@gla.ac.in

Abstract

Water contaminants represent a significant global challenge that impacts the environment. Research shows that lead exposure may result in urinary, cardiovascular, digestive, respiratory, and neurological disorders. By in-situ polymerizing pyrrole on $CoFe_2O_4$ nanoparticles, a polypyrrole-coated cobalt ferrite (PPy@$CoFe_2O_4$) magnetic nanosorbent is synthesized to achieve efficient removal of Pb(II). XRD data corroborated the findings of the SEM examination, which showed spherical nanoparticles with diameters of about 50 nm. The investigation of zeta potential revealed that the polypyrrole-coated cobalt ferrite nanoparticles have a positive surface charge in an acidic medium and a negative surface charge in alkaline media. The equilibrium time was found to be 70 min, and the adsorption behavior aligned with a pseudo-second-order kinetic model. The adsorption isotherms were accurately represented by the Langmuir model. PPy/$CoFe_2O_4$ demonstrates a maximal monolayer adsorption capacity of 357.14 mg·g^{-1} under optimum conditions (330 K temperature, 0.16 g·L^{-1} adsorbent dose, and pH 8.0). The removal efficiency was still higher than 94% following the five adsorption-desorption cycles. Electrostatic interaction is a primary mechanism influencing Pb(II) adsorption onto the surface of PPy/$CoFe_2O_4$. A negative $\Delta G°$ indicates that Pb(II) adsorption onto PPy/$CoFe_2O_4$ proceeds spontaneously. The results indicate that the PPy/$CoFe_2O_4$ composite functions as a highly efficient adsorbent, showcasing extensive applicability in the treatment of wastewater contaminated with heavy metal ions.

Citation: Srivastava A, Srivastava N, Nayak R, Singh R. 2025. Kinetic and thermodynamic evaluation of adsorptive removal of lead(II) from aqueous solutions using Polypyrrole@$CoFe_2O_4$ nano-adsorbent. *Progress in Reaction Kinetics and Mechanism* 50: e006 https://doi.org/10.48130/prkm-0025-0006

Introduction

The shortage of access to potable water remains a significant challenge in many nations. Approximately 25% of the world's population lack a supply of safe drinking water, resulting in a significant public health crisis that claims 3.4 million lives each year, with children being the most affected due to waterborne diseases[1,2]. The existence of heavy metal ions (HMIs) in water represents a considerable threat to the integrity of water purity and can lead to adverse consequences for biological systems. Even the slightest presence of HMIs may adversely affect living beings[3]. The root cause for this is the significant tendency of HMIs to accumulate within food webs and ecosystems[4]. HMIs are persistent in the environment and exhibit carcinogenic characteristics[5]. About 40% of the surface water on Earth, primarily from rivers and lakes, is tainted by HMIs, largely due to agricultural and industrial activities[6].

Lead is a highly poisonous element that occurs naturally in the Earth's crust[7]. Its pervasive use has resulted in considerable environmental damage and major public health issues across the globe. Recycling activities, manufacturing, smelting, and mining as well as the use of lead in various goods, are significant causes of environmental contamination[8–10]. Infants and kids are more exposed to lead's harmful effects, which can have long-term health consequences, especially related to central nervous system development[11,12]. Lead penetrates the body and is transferred to several organs, including bones, liver, kidneys, and the brain. Lead is retained in bones and teeth, where it gradually accumulates[12]. Lead contained in bone can be discharged into the bloodstream during pregnancy, exposing the fetus, resulting in premature delivery, and decreased fetal growth[13]. The World Health Organization (WHO) specifies that the optimal permissible level of Pb(II) in drinking water is 0.01 mg·L^{-1}[14]. Consequently, it is critical for the public health and environment that lead be removed from contaminated water and wastewater.

Wastewater purification systems may remove up to 80% of pollutants, but this high efficacy is attainable only when combined with sophisticated treatment techniques. Advanced remediation procedures include multiple approaches that involve chemical precipitation, electrodialysis, photocatalysis, adsorption, coagulation, filtration, advanced oxidation processes, membrane separation, ion exchange, and electrocoagulation[15–24]. Within these methodologies, adsorption is recognized as a highly efficient and promising approach due to its straightforward operation, remarkable efficacy, affordability, and minimal generation of residual contaminants[2]. Modified polymers, organic porous frameworks, carbon nanotubes (CNTs), and activated carbon exemplify a range of adsorbents recognized for being efficient in the removal of Pb(II)[25–28]. Nonetheless, these adsorbents present significant limitations in terms of regeneration and separation[29].

Conducting polymers (CPs) contain conjugated π systems and present significant potential in various domains, including gas sensing, corrosion prevention, and biomedicine[2]. Polypyrrole, a type of conducting polymer, provides an efficient and practical strategy for treating wastewater and efficiently eliminating HMIs and other pollutants due to the functional groups on its outer layer and its adaptable properties[2]. While pure conducting polymers possess certain limitations, their amalgamation with different materials to form advanced composites effectively addresses such obstacles. The incorporation of CPs within these composites imparts unique

pH-responsive, mechanical, and electrical properties, rendering them highly effective for treating wastewater[2].

CP-based magnetic nanocomposites (MNCPs) integrate the advantages of their individual components, enhancing adsorption via superparamagnetic and pH-responsiveness properties, thereby enabling easy separation with an exterior magnetic field. The presence of functional groups like –OH, -NH-, -S-, and NH_2 on NCPs enhances the binding of HMIs through a variety of interactions. The MNCPs are highly regarded for their conductance, stability, simplicity in preparation, and effective recuperation, making them exemplary materials for the removal of HMIs from wastewater[2].

This research utilizes a straightforward in situ chemical polymerization approach to synthesize an innovative polypyrrole-coated cobalt ferrite magnetic nano adsorption material (PPy/$CoFe_2O_4$). The PPy/$CoFe_2O_4$ nanocomposites underwent thorough characterization through a range of techniques, such as Fe-SEM, XRD, and FTIR, while their efficacy in adsorbing Pb(II) from synthetic aqueous samples was meticulously assessed. Evaluations were conducted to assess the capacity of pure cobalt ferrite nanoparticles, pristine polypyrrole, and PPy/$CoFe_2O_4$ nanocomposite to adsorb Pb(II). Through instrumental studies and adsorption investigations, we propose the most probable mechanistic pathway for the adsorptive elimination of Pb(II) utilizing the PPy/$CoFe_2O_4$ composites. While there exists a plethora of reports concerning the removal of Pb(II) from water-based solutions[12–24] they reveal limitations in terms of adsorption capacity and present significant challenges in regeneration. Considering the aforementioned facts, the developed PPy@$CoFe_2O_4$ nanocomposite presents a wide array of advantages, including excellent adsorption capacity, enhanced separability, suitability for HMIs, and economic viability. The goal of the current study is to determine the optimal parameters for the removal of Pb(II), in line with research on actual wastewater treatment. The pH responsiveness of the synthesized nanocomposite renders it an appropriate candidate for the efficient removal of HMIs, as well as both cationic and anionic dyes from wastewater.

Experimental

Reagents and equipment

This study employed analytical-quality $Fe(NO_3)_3{\cdot}9H_2O$, (≥ 99% pure) and $Co(NO_3)_2{\cdot}6H_2O$, (≥ 99% pure) obtained from Himedia India. Chemicals acquired include lead(II) nitrate from Merck India, sodium dodecyl sulfate (SDS), ammonium persulfate (98%), sucrose ($C_{12}H_{22}O_{11}$), nitric acid (HNO_3), and monoethanolamine (C_2H_7NO) 99% Pure, from SRL, pyrrole (99% pure) from Spectrochem India. The Pb(II) supply solution was prepared using highly purified water, achieved through the process of double distillation of deionized water.

Employing a FE-SEM (Nova NanoSEM 450), the morphologies of PPy/$CoFe_2O_4$ and $CoFe_2O_4$ were analyzed. A digital pH meter from Ohaus (model OH30057496) was employed to determine the pH of the solution being investigated. The IRTracer-100 FTIR spectrometer (Shimadzu, Japan) was employed to acquire the FTIR spectra of PPy/$CoFe_2O_4$ and $CoFe_2O_4$, applying KBr pellets for the analysis. In the 2θ range of 20° to 80°, PPy/$CoFe_2O_4$, and $CoFe_2O_4$ X-ray diffraction (XRD) patterns were analyzed employing a D/MAX-2500PCX diffractometer equipped with Cu$K\alpha$ radiation. After adsorption trials, the Pb(II) content was measured by PerkinElmer atomic absorption spectrometer (PinAAcle 900 Series AA). The zeta potential of the composite was evaluated using the Malvern Zetasizer.

Preparation of $CoFe_2O_4$ nanoparticles

Spherical cobalt ferrite nanoparticles were prepared utilizing the solution combustion approach[30,31]. At the outset, precise stoichiometric quantities of $Fe(NO_3)_3{\cdot}9H_2O$ and $Co(NO_3)_2{\cdot}6H_2O$ were dissolved in water. Monoethanolamine effectively stabilizes the nanoparticles, preventing accumulation through electrostatic and/or steric stabilization, ensuring a uniform size, and reducing clustering. Sucrose functioned as a source of energy, supplying the requisite heat to initiate the combustion process. Nitric acid, on the other hand, worked as an oxidizing agent, promoting the oxidation of both metal ions and sucrose. The heat produced during the process of oxidation initiated combustion and aided in the decomposition of metal precursors, resulting in the formation of nanoparticles. The mixture was heated and then annealed at 650 °C for 4 h[30,31].

Preparation of PPy/$CoFe_2O_4$ nanocomposite

Employing $(NH_4)_2S_2O_8$ as the oxidizing agent, pyrrole was polymerized on $CoFe_2O_4$ nanoparticles using a chemical oxidative approach at a temperature spanning 0 to 5 °C to synthesize a PPy/$CoFe_2O_4$ composite. After carefully dispersing 0.1 g of prepared $CoFe_2O_4$ in 100 ml of 0.01 M SDS, the sample underwent a 30-min ultrasound treatment utilizing a probe sonicator. Following this, the 0.1 M cooled liquid pyrrole (double-distilled) was carefully introduced into the solution beaker, with constant stirring maintained at 1800 rpm. A solution of $(NH_4)_2S_2O_8$, recognized for its oxidizing characteristics, was added gradually. The stirring process was maintained for 8 h. The two distinct layers thus emerged. The upper layer, distinguished by its lightweight characteristics, is composed solely of PPy, which was extracted via decanting. The layer of reduced density is composed of $CoFe_2O_4$ nanoparticles coated with PPy, which was subsequently filtered, washed using 50% ethanol, and heated at a temperature of 70 °C for 20 h for complete drying[32]. The schematic for the fabrication of $CoFe_2O_4$ nanoparticles and PPy/$CoFe_2O_4$ nanocomposite is illustrated in Fig. 1.

Adsorption investigation

The investigation of Pb(II) adsorption was conducted through batch processes. A 200 mg·L^{-1} solution of lead(II) nitrate was prepared and subsequently diluted to achieve different concentrations. Typically, 0.008 g of PPy/$CoFe_2O_4$ was treated with 50 mL of Pb(II)

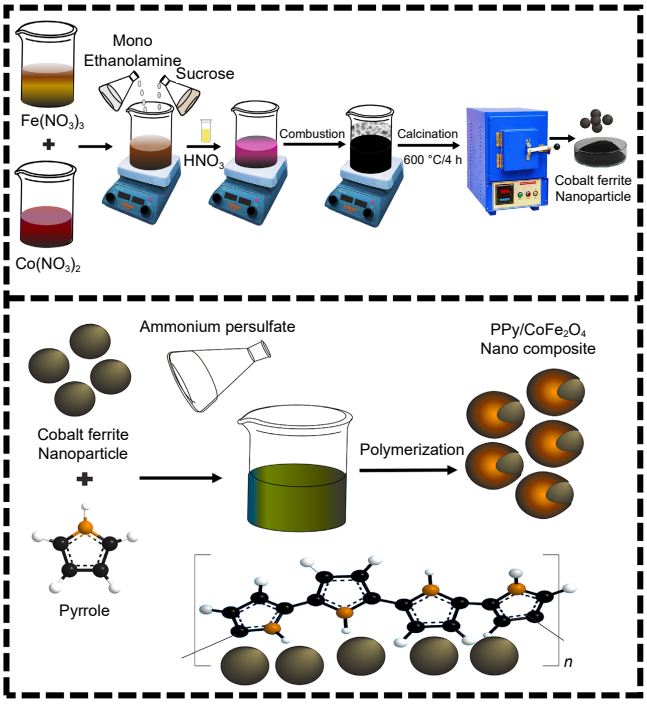

Fig. 1 Schematic for the fabrication of $CoFe_2O_4$ nanoparticles and PPy/$CoFe_2O_4$ nanocomposite.

solution at the designated temperature. At various times, the PPy/$CoFe_2O_4$ was extracted from the solution employing an external magnet, and the remaining content of Pb(II) following adsorption was quantified through atomic absorption analysis. The percentage removal of Pb(II), together with the adsorption of Pb(II) at any given moment and at equilibrium, represented as Q_t (mg·g^{-1}) and Q_e (mg·g^{-1}), respectively, was calculated applying Eqns (1) and (2)[33]. Every experiment was carried out in triplicate.

$$\% \text{ Removal} = \frac{(C_o - C_e)}{C_o} \times 100 \quad (1)$$

$$Q_e = \frac{(C_o - C_e) \times V}{m} \quad (2)$$

The adsorbent's mass (m), the solution's volume (V), the equilibrium concentration of Pb(II) (C_e), and the initial concentration of Pb(II) (C_o), are among the variables. The optimal settings for the removal of Pb(II) were determined through a comprehensive analysis of various factors, including temperature (298–318 K), contact time (2–120 min), adsorbent quantity (0.04–0.30 g·L^{-1}), pH (2.0–12.0), and Pb(II) concentration via batch trails.

PPy/$CoFe_2O_4$ nanocomposite regeneration

The desorption, merely the reverse of the adsorption process, encompasses the discharge of a material that was initially adsorbed to the exterior of the adsorbent. This study represented five cycles of adsorption and desorption utilizing the PPy/$CoFe_2O_4$ nanocomposite. Every cycle involved adding 0.008 g of the PPy/$CoFe_2O_4$ to a glass vessel comprising 50 mL of a Pb(II) solution (30 mg/L), keeping the temperature at 30 °C, agitating at 250 rpm, and maintaining a controlled pH of 8.0. The remainder of the Pb(II) concentration in the solution was assessed subsequent to agitation. The residual material underwent a meticulous cleaning process with distilled water before drying at 110 °C for 11 h, facilitating subsequent desorption experiments.

The Pb(II) desorption from the PPy/$CoFe_2O_4$ surface was examined using various solvents such as HCl, H_2SO_4, methanol, and ethanol. The desorption procedure entailed submerging the depleted PPy/$CoFe_2O_4$ in 50 mL of various solvents and agitating the mixture at 25 °C for a duration of 2 h. The adsorbent was then subjected to a rinsing process using distilled water to remove any residual solvent, followed by drying for 11 h at 110 °C. The concentration of leftover Pb(II) was measured following the completion of the desorption study. The efficiency of desorption, as defined by Eqn (3), represents the proportion of pollutants that have been desorbed relative to the initial amount adsorbed, thereby providing valuable insights into the reuse ability and rejuvenating capabilities of the nanocomposite[34].

$$\% \text{ Desorption} = \frac{M_{ads}}{M_{des}} \times 100 \quad (3)$$

The total quantity of Pb(II) adsorbed and desorbed in mg·L^{-1} is denoted by M_{ads} and M_{des}, correspondingly.

Results and discussion

Evaluation of synthesized $CoFe_2O_4$ nanoparticle and polypyrrole coated $CoFe_2O_4$ nanocomposite

X-ray diffraction assessment

The examination of the composition and crystal structure of the PPy/$CoFe_2O_4$ composite and $CoFe_2O_4$ nanoparticles was performed utilizing X-ray diffraction (XRD), as depicted in Fig. 2a. The XRD pattern clearly demonstrates five distinctive spikes at 62.6°, 56.95°, 53.05°, 43.05°, 35.4°, and 30° corresponding to the (440), (511), (422), (400), (311), and (220) planes of $CoFe_2O_4$, respectively[35,36]. The PPy/$CoFe_2O_4$ composite and $CoFe_2O_4$ nanoparticles were found to have crystallite diameters of 18.0 and 17.5 nm, respectively, computed utilizing the Debye-Scherrer equation. The distinct and prominent XRD peaks of $CoFe_2O_4$ confirm the enhanced crystallization of the nanoparticles. The observed decrease in peak intensity levels of the PPy/$CoFe_2O_4$ indicates that PPy efficiently envelops the surface of the $CoFe_2O_4$ nanoparticles. Moreover, distinctive peaks regarding PPy were identified within the spectrum ranging from 25° to 27°, and were in close agreement with the findings of previous research[37].

SEM analysis

A structural investigation employing scanning electron microscopy uncovered uniformly distributed cobalt ferrite nanoparticles with a diameter spanning from 20 to 50 nm (Fig. 2b). The interactions between magnetic dipoles lead to significant accumulation; however, the individual particles retain their distinct shapes, indicating minimal integration. The measured surface roughness reflects the effective synthesis of cobalt ferrite, characterized by a consistent morphology and size distribution. This indicates that meticulous oversight of precursor concentration and the strategic alteration of reaction conditions governed the synthesis process. A delicate layer of PPy uniformly envelops the core-shell architecture of $CoFe_2O_4$ nanoparticles, as observed in the SEM images of the PPy/$CoFe_2O_4$ composite. This coating increases the diameter of the particles to a range of 50–100 nm and triggers particle accumulation (Fig. 2c). The astonishingly sleek layer of PPy on cobalt ferrite, along with the hydrophobic and Vanderwaal interactions among the polypyrrole molecules, could potentially explain the observed agglomeration. The homogeneous surface structure of the

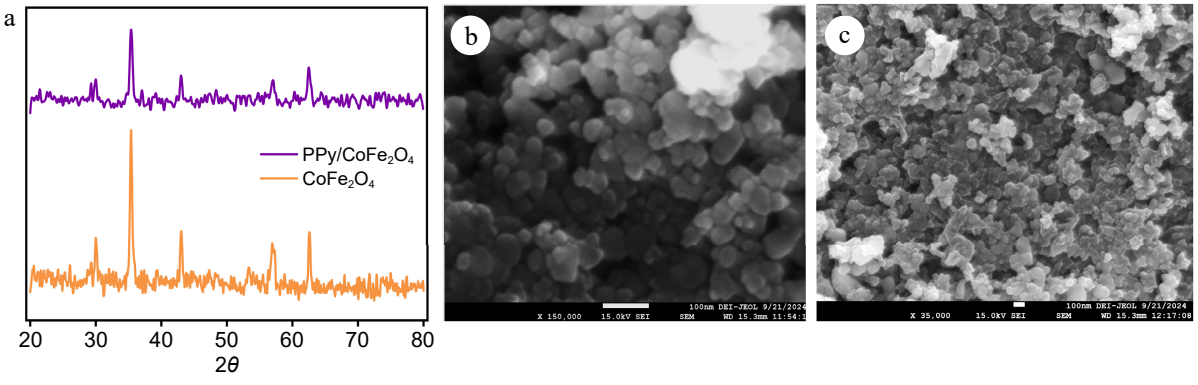

Fig. 2 (a) X-ray diffraction patterns of cobalt ferrite and polypyrrole coated cobalt ferrite nanocomposite. (b) FE-SEM image of cobalt ferrite. (c) FE-SEM image polypyrrole coated cobalt ferrite.

$PPy/CoFe_2O_4$ composite supports the effectiveness of the in situ polymerization process.

FTIR assessment

The FTIR spectrum of $CoFe_2O_4$ nanoparticles reveals distinctive vibrational modes, indicating the existence of the spinel structure (Fig. 3a). The two primary bands recognized in the majority of spinel ferrites are apparent across the spectrum of 400–600 cm^{-1}. The peak noticed at 541 cm^{-1} is indicative of Fe-O bending vibrations occurring within the tetrahedral sites. While the peaks observed at 461 cm^{-1} correspond to Co-O bending (octahedral sites)[38]. The observation of the supplementary band at 3,747 cm^{-1} (stretching vibrations) suggests the presence of O-H group[39]. The peak identified at 2,361 cm^{-1} could plausibly be associated with organic leftovers found in the material[40]. The development of the spinel ferrite framework is confirmed by the presence of these absorption bands. With the inclusion of PPy, the 461 cm^{-1} peak undergoes a shift to 467 cm^{-1}, while the 541 cm^{-1} peak transitions to 562 cm^{-1}[37]. The interaction between PPy and $CoFe_2O_4$ is the primary cause of the observed transformation. The distinctive absorption band in $PPy/CoFe_2O_4$, identified at 3,438 cm^{-1}, can be attributed to the stretching vibrations of O-H and N-H. The spectral signature detected at 758 cm^{-1} is associated with PPy's C-H wagging mode[41]. The bands identified at 1,038 and 915 cm^{-1} are caused by vibrations correlated with the N-H in-plane deformation and the C-H deformation found in the pyrrole ring, respectively[42,43]. The bands at 1,462, 1,541, and 1,652 cm^{-1} correspond to the C-C, C=C, and C=N groups in Ppy[41,43]. The FTIR peaks observed within the range of 2,845–2,971 cm^{-1} in $PPy/CoFe_2O_4$ and $CoFe_2O_4$ indicate the presence of C-H str. vibrations associated with the alkyl groups intrinsic to the PPy skeleton or arising from leftover organic compounds utilized in the synthesis[43].

Zeta-potential study

$PPy/CoFe_2O_4$'s PZC (point of zero charge) was determined by adding 20 mL of NaCl (0.1 M) to a conical flask. The pH of the solution was maintained within the range of 2 to 12 utilizing 0.1 M NaOH or 0.1 M HCl. Following the incorporation of $PPy/CoFe_2O_4$ (0.008 g), we meticulously sealed the flasks and allowed the contents to equilibrate at room temperature for a duration of 2 d. The Malvern Zetasizer was employed to measure the zeta potential of the prepared samples. The PZC of $PPy/CoFe_2O_4$ can be examined to have a better understanding of the effect of pH. In the current context, the $PPy/CoFe_2O_4$'s PZC was determined to be 6.5, indicating that for pH levels higher than 6.5, its exterior displays a negative charge (Fig. 3b).

Impact of pH on the removal of Pb(II)

The primary determinant influencing the efficacy of adsorption is pH, as it alters the interfacial properties of both the adsorbent and adsorbate. This alteration influences the conduct of the adsorbate within the reaction mixture, along with the protonation or deprotonation of various functional groups present on the exterior of the adsorbent. The impact of the solution's pH on Pb(II) adsorption is influenced by several parameters. The electrostatic interaction among the adsorbent and adsorbate constitutes a critical consideration in the analysis.

The examination of Pb(II) adsorption on $PPy/CoFe_2O_4$ was carried out over a pH spectrum of 2.0–12.0, as illustrated in Fig. 4. The results reveal that as the pH transitions from 2.0 to 12.0, the adsorption capacity for Pb(II) increases significantly, from 53.18 to 185.94 $mg{\cdot}g^{-1}$ (23.36% to 99.17% removal). With an increase in the pH level, the electrostatic interactions among $PPy/CoFe_2O_4$ and Pb(II) become more pronounced, resulting in enhanced adsorption capabilities.

At low pH, Pb(II) competes with H^+ ions for the adsorbent's active sites, causing these sites to become protonated. Consequently, the Pb(II) and adsorbent undergo diminished columbic interactions, leading to a reduction in adsorption efficiency. The adsorption is observed to intensify as the pH of solutions rises. Deprotonation of the Fe–OH and -C=N–H groups occurs at about neutral pH values, resulting in the generation of Fe–O and -C=N, which demonstrate improved interactions with Pb(II).

The influence of pH can be examined in greater depth by evaluating the PZC of $PPy/CoFe_2O_4$[44]. In the current context, $PPy/CoFe_2O_4$'s PZC was found to be 6.5 (Fig. 3b), indicating that for pH values higher than 6.5, its exterior exhibits a negative charge. This finding is consistent with the prevailing concept that increased negative charge on the surface at higher pH results in greater attraction between the positively charged Pb(II) and adsorbent. Subsequently, experiments were performed at pH 8.0. A comparable trend of alteration in adsorbent capability concerning pH has been documented for the Pb(II) removal[45,46].

Impact of $PPy/CoFe_2O_4$ dose on the adsorption capacity and % removal of Pb(II)

The proportion of adsorbent to adsorbate plays a crucial role in the overall adsorption process, and the optimization of adsorption is frequently aligned with the quantity of adsorbent utilized within a defined volume of adsorbate solution. Figure 5 illustrates the influence of varying adsorbent doses on the effectiveness of Pb(II) removal. As the adsorbent dose escalates from 0.04 to 0.30 $g{\cdot}L^{-1}$, a notable enhancement in removal efficiency is observed, advancing from 72.67% to 99.0%. A larger surface area and more active sites

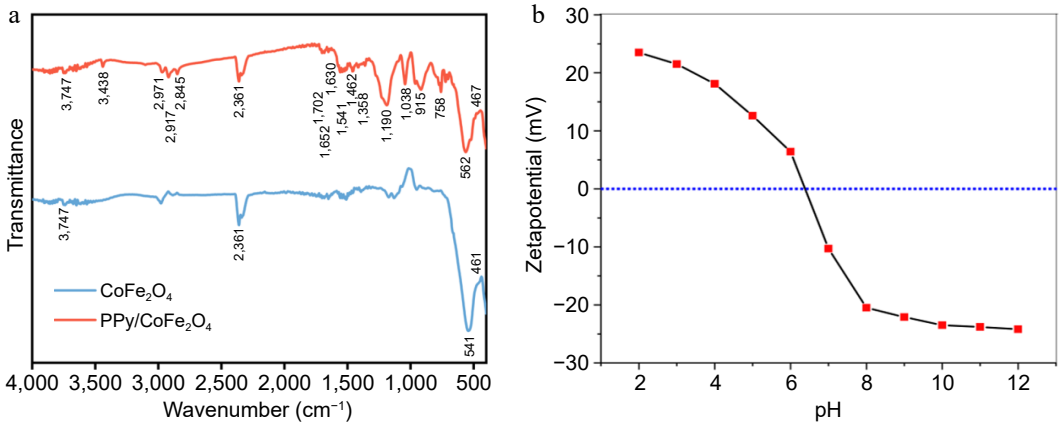

Fig. 3 (a) FTIR spectrum of synthesized $PPy/CoFe_2O_4$ and $CoFe_2O_4$. (b) pH's influence on $PPy/CoFe_2O_4$'s zeta-potential.

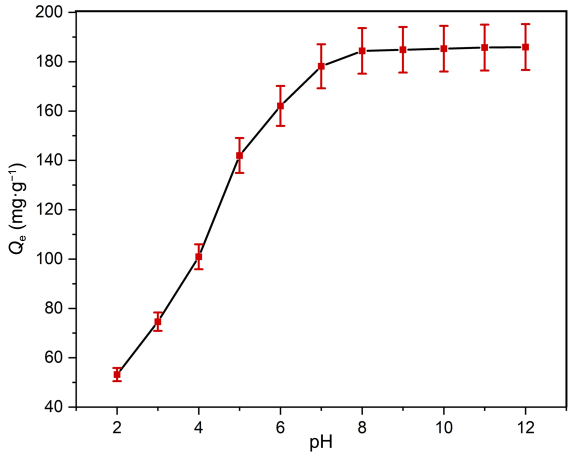

Fig. 4 Impact of pH on adsorption capability of Pb(II) at contact time = 120 min, adsorbent dose = 0.16 g·L^{-1}, T = 303 K, and Pb(II)] = 30 mg·L^{-1}.

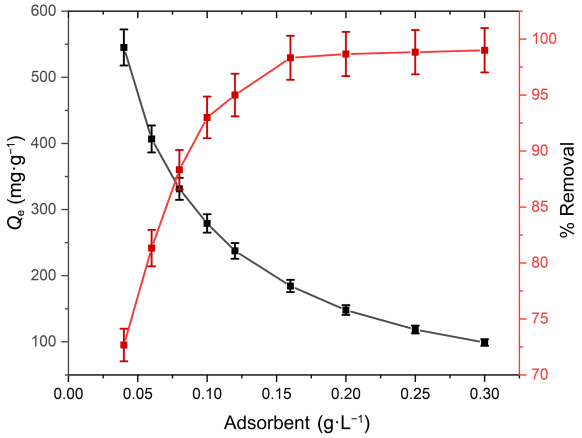

Fig. 5 Impact of adsorbent dose on adsorption capacity and % removal Pb(II) at contact time = 120 min, T = 303 K, pH = 8.0, and [Pb(II)] = 30 mg·L^{-1}.

accessible for adsorption are liable for the enhancement in removal efficiency. The removal efficiency attains a plateau beyond this threshold, as the Pb(II) concentration emerges as the limiting factor. With increasing adsorbent dosage, Pb(II) adsorption capability decreased (545 to 99 mg·g^{-1}). Increased adsorbent dosage may provide more active adsorption sites, which remain unsaturated following adsorption, decreasing adsorption capacity. This reduction may also be ascribed to a diminished surface area and an extended diffusion path length, which arises from the agglomeration of adsorption sites[45,46]. The results highlight the pronounced capability of PPy/$CoFe_2O_4$ nanomaterial in the removal of Pb(II).

Impact of Pb(II) content and contact duration on the removal of Pb(II)

The effect of equilibrium time is an important parameter for designing a low-cost wastewater treatment system[47]. The study examined the adsorption ability of Pb(II) on the PPy/$CoFe_2O_4$ composite over a specified time period to ascertain the point of equilibrium. Every experiment was meticulously replicated in triplicate to assure consistency. Figure 6a demonstrates how the adsorption capability of PPy/$CoFe_2O_4$ is affected by the time of contact and the initial concentrations of Pb(II) (15, 30, and 60 mg·L^{-1}). The initial phase of Pb(II) adsorption exhibited a swift increase, largely attributed to the plentiful active binding sites instantly accessible on the exterior of the nanocomposite. Nonetheless, over time, the rate of adsorption gradually decreased. The diminished number of accessible active sites, coupled with the extended diffusion paths that adsorbate moieties are required to traverse in the later stages of the process, serves as the rationale for the observed deceleration. The adsorption process commenced with a swift initial phase, subsequently evolving into a more gradual removal stage, ultimately culminating in a state of equilibrium. The PPy/$CoFe_2O_4$ composite displayed its maximal adsorption capacity for Pb(II) within 70 min, suggesting that a state of equilibrium has been primarily achieved. The rapid adsorption noticed can be ascribed to the easily attainable architecture of the PPy/$CoFe_2O_4$ composite, suggesting that the majority of adsorption sites are located on the outer surface, facilitating swift interactions with Pb(II). At a starting concentration of 30 mg·L^{-1}, the PPy/$CoFe_2O_4$ composite effectively adsorbed Pb(II) from an aqueous solution, reaching equilibrium in 70 min. Significantly, around 92.5% of Pb(II) was removed within the initial 20 min, underscoring the composite's effectiveness and swift performance.

The PPy/$CoFe_2O_4$ composite achieved adsorption equilibrium for Pb(II) removal within 70 min, showcasing an impressive removal efficacy of around 98.3%, compared to the 79.8% noted for $CoFe_2O_4$ nanoparticles under identical circumstances. The removal efficiency of polypyrrole nanostructures, on the other hand, was only 63.9% over the same period of time. Pb(II) will be removed more effectively by the PPy/$CoFe_2O_4$ composite when contrasted with $CoFe_2O_4$ and PPy (Fig. 6b).

Kinetics examination

Assessments that account for temporal variables were undertaken to explore the kinetics of adsorption. Intraparticle diffusion (IPD) model (Eqn 4), Ho-McKay's second-order kinetic model (Eqn 5), and Lagergren's first-order model (Eqn 6) were employed to examine the experiment's temporal data. In this context, k_p (mg·g^{-1}·min$^{-0.5}$), k_2 (g^{-1}·mg^{-1}·min^{-1}), and k_1 (min^{-1}) represent the rate constants associated with the intraparticle diffusion, pseudo-second-order, and pseudo-first-order respectively. Table 1 presents a comprehensive summary of the parameters calculated for these models.

$$Q_t = k_p t^{1/2} + C \tag{4}$$

$$\frac{t}{Q_t} = \frac{t}{Q_e} + \frac{1}{k_2 Q_e^2} \tag{5}$$

$$\log(Q_e - Q_t) = \log Q_e - \frac{k_1}{2.303} t \tag{6}$$

Here, Q_e (mg·g^{-1}) and Q_t (mg·g^{-1}) represent the amount of Pb(II) that has been adsorbed onto PPy/$CoFe_2O_4$ at equilibrium, and at a specific time t, respectively. Additionally, k_p signifies the constant associated with intraparticle diffusion, while C indicates the intercept value.

The omission of Pb(II) demonstrates a strong correlation with the pseudo-second-order model (PSO), showcasing R^2 values approaching 1. An examination of the regression coefficients indicates that R^2 attains 0.9995 value in the context of PSO kinetics analysis (Fig. 7b). In contrast, when applying the pseudo-first-order kinetic model (PFO), the R^2 value was determined to be 0.9582 (Fig. 7a). The adsorption capacity determined through the PSO model (357.1 mg·g^{-1}) is in close alignment with the experiment's findings (343.2 mg·g^{-1}), particularly when juxtaposed with the PFO model (173.3 mg·g^{-1}). The findings indicate that the kinetics of Pb(II) adsorption on PPy/$CoFe_2O_4$ adhere to the principles of second-order kinetics. For the removal of Pb(II), analogous pseudo-second-order kinetic action has also been observed with Polyaniline/Fe_3O_4[45], Polythiophene-Coated Rice Husk[46], and Polyaniline Sn(IV) tungstomolybdate nanocomposite[48].

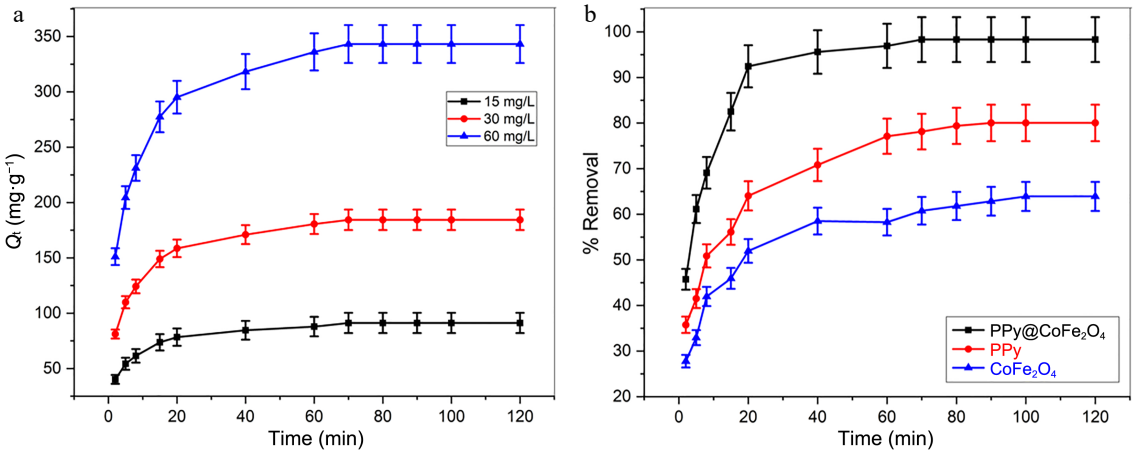

Fig. 6 (a) Impact of [Pb(II))] and contact duration on adsorption capability of Pb(II) at contact time = 120 min, T = 303 K, pH = 8.0, and adsorbent dose = 0.16 g·L^{-1}. (b) Analysis of the efficacy of Pb(II) removal utilizing PPy/$CoFe_2O_4$, PPy, and $CoFe_2O_4$ at contact time = 120 min, adsorbent dose = 0.16 g·L^{-1}, T = 303 K, pH = 8.0, and [Pb(II)] = 30 mg·L^{-1}.

Table 1. Variables computed from the PSO, and PFO kinetic model.

Kinetic models	Variables	Initial Pb(II) content (mg·l^{-1})		
		15	30	60
Pseudo-first order kinetic	Q_e (mg·g^{-1})	42.26	93.60	173.27
	R^2	0.9582	0.9797	0.9672
	k_1 (min^{-1})	0.0552	0.0532	0.0531
Pseudo-second order kinetic	k_2 (g^{-1}·mg^{-1}·min^{-1})	3.07×10^{-3}	1.43×10^{-3}	7.54×10^{-4}
	Q_e (mg·g^{-1})	92.59	188.68	357.14
	R^2	0.9995	0.9991	0.9989
Q_e (mg·g^{-1}) [Experimental]		91.2	184.4	343.2

The mechanism of Pb(II) adsorption onto PPy/$CoFe_2O_4$ was better understood through the application of the IPD model, which was obtained by plotting $t_{1/2}$ vs Q_t. As illustrated in (Fig. 7c), the adsorption process proceeds via two linear pathways. The initial linear segment illustrates the predominance of mass transfer; wherein metal ions (Pb(II)) migrate from the bulk solution to the surface of the adsorbent. The second linear section reflects diffusion control, indicating the movement of Pb(II) ions from the surface into the inner pores of the adsorbent. However, it appears that IPD may not serve as the primary reason behind the Pb(II) adsorption onto the PPy/$CoFe_2O_4$ surface, as the linear representations do not intersect at the origin.

Thermodynamic study

The parameters of thermodynamics play a pivotal role in delineating the attributes and viability of the adsorption procedure. The percentage of Pb(II) removal and the capacity for adsorption onto PPy/$CoFe_2O_4$ exhibit a notable decrease as the temperature rises. Equations (7) to (9) were utilized to examine the thermodynamic parameters associated with the adsorption of Pb(II) on PPy/$CoFe_2O_4$ within a temperature spectrum of 298 to 318 K. Equation 7 delineates the relationship between enthalpy (ΔH°) and entropy (ΔS°) of adsorption in relation to ΔG°. Conversely, Eqn 8 presents the formulation for K_D. Gibbs free energy change (ΔG°) and the equilibrium constant (K_D) at a particular temperature (T) is established by Eqn (9).

$$\ln K_D = -\left(\frac{\Delta G^o}{RT}\right) = -\left(\frac{\Delta H^o}{RT}\right) + \left(\frac{\Delta S^o}{R}\right) \quad (7)$$

$$K_D = \frac{C_{Ae}}{C_e} \quad (8)$$

$$\Delta G° = -RT\ln K_D \quad (9)$$

The content of Pb(II) at equilibrium is denoted as C_e, while the amount of Pb(II) that is adsorbed on PPy/$CoFe_2O_4$ at equilibrium is represented as C_{Ae}. The intercept and slope of the lnK_D vs 1/T plot provided the values for ΔH° and ΔS°. The computed values of the different variables have been encapsulated in Table 2.

The negative ΔH° value indicates that Pb(II) undergoes exothermic adsorption onto the surface of PPy/$CoFe_2O_4$. Furthermore, the negative ΔG° substantiates that the Pb(II) adsorption onto PPy/$CoFe_2O_4$ transpires spontaneously. As the temperature increases, the adsorption becomes more effective, as indicated by the reducing ΔG° values. During adsorption, the solid-solution interface appears to have less randomness, as indicated by the negative ΔS° value. Studies utilizing Polyaniline/Fe_3O_4, and Polythiophene-Coated Rice Husk as adsorbents have demonstrated comparable patterns of enthalpy and entropy during the removal of Pb(II)[46,47].

Adsorption isotherms

The selection of a suitable isotherm model is essential for comprehending and enhancing the processes of adsorption. The Pb(II) adsorption results on PPy/$CoFe_2O_4$ at equilibrium were subjected to analysis through the application of several isotherm models, notably Langmuir, Temkin, and Freundlich. The Freundlich model elucidates the phenomenon of multilayer adsorption, highlighting a spectrum of affinity and energies of adsorption available on a heterogeneous exterior. Conversely, the Langmuir model posits that adsorption occurs in a monolayer at a predetermined number of unified, energetically comparable sites, with negligible interactions between the molecules adsorbed. The Temkin model asserts that as surface coverage expands, there is a linear decline in the heat of adsorption for every single molecule within the layer due to the interactions between the adsorbent and adsorbate.

Langmuir's adsorption equation delineates the relationship for a monolayer of adsorbate that adheres to the exterior of an adsorbent characterized by a limited number of active sites, and can be expressed as[49]:

$$\frac{C_e}{Q_e} = \frac{1}{Q_{max}K_L} + \frac{C_e}{Q_{max}} \quad (10)$$

Here, the Pb(II) concentration at equilibrium is expressed as C_e (mg·L^{-1}), Q_{max} (mg·g^{-1}) represents the monolayer adsorption capacity, the amount of Pb(II) adsorbed at equilibrium on PPy/$CoFe_2O_4$ is designated by Q_e (mg·g^{-1}), and K_L (l·mg^{-1}) described the Langmuir constant. The free energy associated with the adsorp-

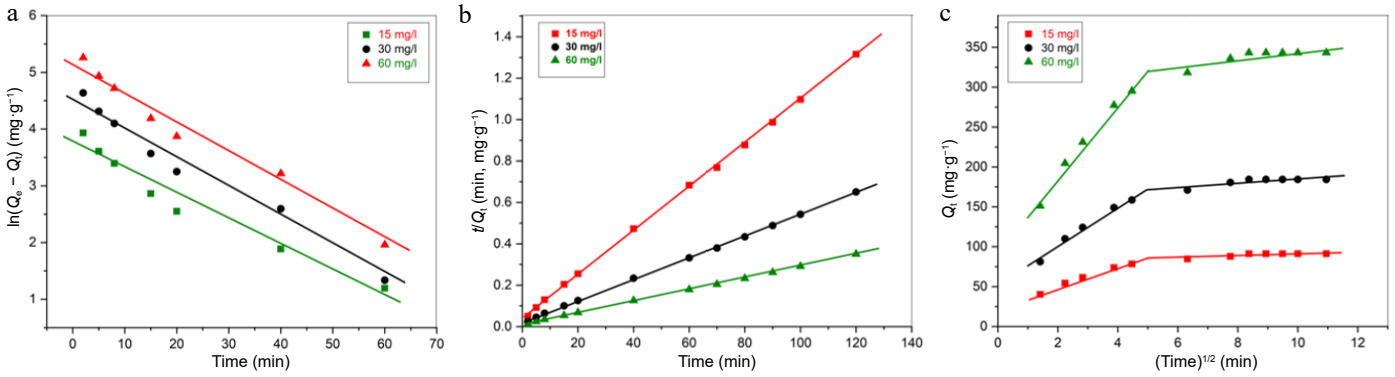

Fig. 7 (a) PFO kinetic study, (b) PSO kinetic study, (c) IPD diffusion kinetic study for adsorption of Pb(II) by PPy/$CoFe_2O_4$ at contact time = 120 min, T = 303 K, pH = 8.0, [Pb(II)] = 30 mg·L^{-1}, and adsorbent dose = 0.16 g·L^{-1}.

Table 2. Thermodynamic variables for adsorptive removal of Pb(II) by PPy/$CoFe_2O_4$.

Temp (K)	$\Delta S^{\#}$ (kJ·$mole^{-1}$)	$\Delta H^{\#}$ (J·K^{-1} $mole^{-1}$)	$\Delta G^{\#}$ (kJ·$mole^{-1}$)
298	−128.2	− 42.2	− 2.4
303			− 3.3
308			− 4.5
313			− 5.5
318			− 6.6

tion phenomena can be explained by the Langmuir constant. Figure 8a presents a graph depicting the relationship between C_e and C_e/Q_e, illustrating a linear correlation. The values of Q_{max} and K_L can be determined through an examination of the slope and intercept of the plot (Table 3). The Langmuir model's validity is strongly supported by the linearity depicted in the plot in Fig. 8a. The results of the experiment demonstrated the uniform properties of the PPy/$CoFe_2O_4$ surface and were in agreement with the Langmuir model. The findings further elucidated the adherence of an exclusive layer (chemisorption) of Pb(II) molecules to the exterior surface of PPy/$CoFe_2O_4$. The prior analysis regarding the Pb(II) adsorption onto Polyaniline/Fe_3O_4[45], Polythiophene-Coated Rice Husk[46] yields comparable results. The outcomes of the current investigation reveal an enhanced capacity for monolayer adsorption of Pb(II) in comparison to the values documented in earlier studies, as outlined in Table 4.

The equation presented below defines a dimensionless equilibria variable, R_L, utilized for evaluating the favorability of adsorption.

$$R_L = \frac{1}{K_L C_o + 1} \tag{11}$$

Here, K_L (l·mg^{-1}) described the Langmuir constant, while the Pb(II) initial concentration is expressed as C_o (mg·L^{-1}). The classification of isotherm types is determined by the R_L value: linear (R_L = 1), favorable (0 < R_L< 1), unfavorable (R_L = 0), or irreversible (R_L > 1)[57].

Instead of describing a plateau-type saturation, the Freundlich model explains multi-layer adsorption, which is more appropriate for heterogeneous surfaces[58]. The expression can be articulated mathematically as:

$$\log Q_e = \frac{1}{n}\log C_e + \log K_F \tag{12}$$

Where, the Pb(II) concentration at equilibrium is expressed as C_e (mg·L^{-1}), and the amount of Pb(II) adsorbed at equilibrium on PPy/$CoFe_2O_4$ is designated by Q_e (mg·g^{-1}). Additionally, n and K_F denote the specific constants associated with the Freundlich model. The linear relationship between $\ln Q_e$ and $\ln C_e$ can be witnessed in Fig. 8b. The slope (1/n) and intercept ($\ln K_F$) of the graph were utilized to calculate the values of n and K_F, as demonstrated in Table 3. The favorability of adsorption is indicated by the value of n. The Pb(II) adsorption on PPy/$CoFe_2O_4$ aligns with a conventional Langmuir isotherm, as evidenced by the 1/n < 1[49].

The Temkin isotherm model offers substantial comprehension regarding the heat of adsorption, demonstrating a linear decline as the coverage of the adsorbent's surface increases. The Temkin isotherm's linear formulation could be presented as[58]:

$$Q_e = B\ln C_e + B\ln K_T \tag{13}$$

The equilibrium binding constant (K_T) pertains to the maximum binding energy, while the Temkin constant (B J·mol^{-1}) is associated

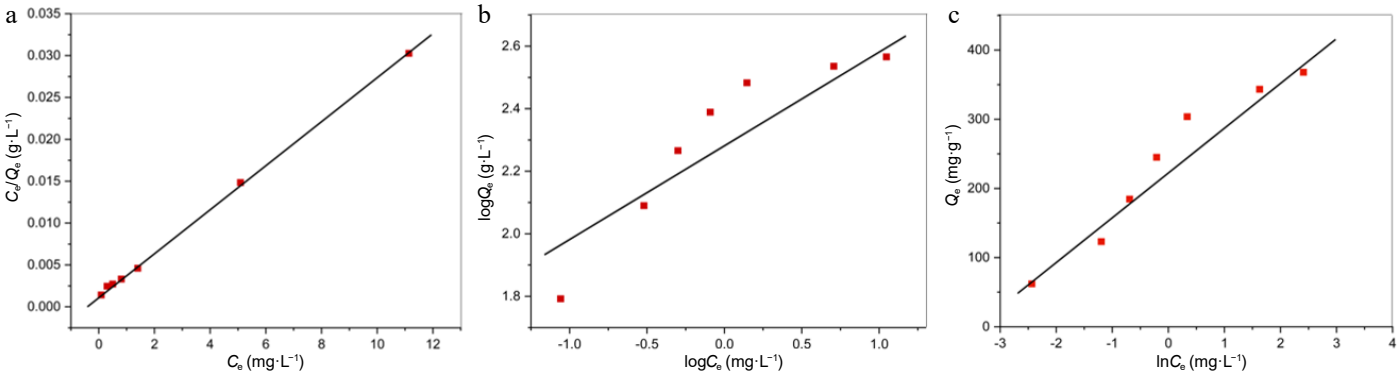

Fig. 8 (a) The relationship between C_e and C_e/Q_e (Langmuir model). (b) The relationship between $\log C_e$ and $\log Q_e$ (Freundlich model). (c) The relationship between $\ln C_e$ and Q_e (Temkin model).

Table 3. Freundlich, Langmuir, and Temkin isotherm constants.

Isotherm	Constant values
Freundlich	K_F ($mg{\cdot}g^{-1}$) = 202.63; 1/n = 0.361; R^2 = 0.8592
Langmuir	R_L = 0.044 – 0.007; R^2 = 0.9995; K_L ($L{\cdot}mg^{-1}$) = 2.15; Q_{max} ($mg{\cdot}g^{-1}$) = 357.14
Temkin	B = 67.30; K_T ($L{\cdot}g^{-1}$) = 32.46; R^2 = 0.9415

Table 4. Competitive assessments of the adsorption capabilities of Pb(II) onto diverse adsorbent materials.

Adsorbent	pH	Contact time (min)	Q_{max} ($mg{\cdot}g^{-1}$)	Ref.
Polyaniline/Fe_3O_4	9.0	120	111.11	[45]
Polythiophene-coated rice husk ash nanocomposite	4.0	240	34.48	[46]
Polyaniline Sn(IV) tungstomolybdate nanocomposite	6.0	60	44.64	[48]
Fig sawdust activated carbon	4.0	120	80.64	[50]
Sulfonated magnetic nano particle	7.0	1440	108.93	[51]
Poly(acrylic acid)/bentonite nanocomposite	--	1440	93.01	[52]
Amino-functionalized magnetic nanoadsorbent	5.0	60	40.1	[53]
Ti(IV) iodovanadate cation exchange	6.0	120	18.8	[54]
Palygorskite-iron oxide nanocomposite	5.0	720	26.7	[55]
Chitosan-starch composite	3.46	300	99.01	[56]
PPy/$CoFe_2O_4$	8.0	120	357.14	This work

with the heat of adsorption. Figure 8c illustrates the correlation between Q_e and lnC_e, which was employed to determine the K_T and B values. Table 3 summarizes the values obtained using the Temkin isotherm.

A significant R^2 value of 0.9995 demonstrates that the Pb(II) adsorption onto PPy/$CoFe_2O_4$ aligns closely with the Langmuir isotherm model. This pronounced correlation indicates a uniform allocation of active adsorption sites throughout the PPy/$CoFe_2O_4$ exterior. Furthermore, the Freundlich constant 1/n was below one, while the constant R_L varied between 0 to 1, suggesting that the adsorption process is thermodynamically favorable. A contrasting evaluation of Pb(II)'s adsorption capability on PPy/$CoFe_2O_4$ relative to various other adsorbents is presented in Table 4. The significant adsorption capacity demonstrated in this investigation underscores the efficacy of PPy/$CoFe_2O_4$ as a viable adsorbent for the omission of Pb(II).

Adsorptive removal mechanism of Pb(II)

Understanding the procedure of adsorbate adherence to the adsorbent surface necessitates a thorough understanding of the mechanisms of interaction that facilitate the elimination of Pb(II) from aqueous solutions. Before elucidating the absorption mechanism, it is imperative to consider both the intrinsic characteristics and the surface attributes of PPy/$CoFe_2O_4$. The columbic interaction between Pb(II) and the de-protonated groups (Fe-OH and –C=N-H) of PPy/$CoFe_2O_4$ at high pH levels elucidates the impact of pH on Pb(II) adsorption outcomes. The results of the zeta potential study can be employed to elucidate the theory of electrostatic interactions. The Pb(II) interacts electrostatically with the adsorbent's negatively charged surfaces when the pH falls above the isoelectric point. Below the isoelectric point, both the adsorbate and the adsorbent have positive charges, resulting in electrostatic repulsion and decreased Pb(II) adsorption. Consequently, considering the impact of the solution's pH on the Pb(II) adsorption, one can hypothesize that the predominant mechanism governing the Pb(II) adsorption onto the surface of PPy/$CoFe_2O_4$ is probably electrostatic interaction.

Regeneration and sustainability

For industrial applications, adsorbents' robustness and versatility are crucial. The desorption of Pb(II) from the surface of PPy/$CoFe_2O_4$ was checked with different solvents including ethanol (99%), methanol (99%), HCl (0.2 M), and H_2SO_4 (0.2 M). Results showed that H_2SO_4 is the best solvent for removing Pb(II) from PPy/$CoFe_2O_4$ (Fig. 9a). Adsorption-desorption investigations were carried out over five successive cycles to evaluate the regeneration capability of PPy/$CoFe_2O_4$. A 0.2 M solution of H_2SO_4 was utilized as the eluent. Specifically, after attaining optimum Pb(II) adsorption, 0.008 g of PPy/$CoFe_2O_4$ was incorporated into 50 mL of H_2SO_4 and swirled until Pb(II) was no longer detectable. The rejuvenated PPy/$CoFe_2O_4$ was thereafter utilized in further cycles. Figure 9b illustrates that the percentage removal of Pb(II) was reduced from 98.3% to 94.8% after five consecutive cycles. This demonstrates that PPy/$CoFe_2O_4$ can be effectively re-used up to five times with minimal performance decline, highlighting the material's longevity for treating wastewater. The PPy/$CoFe_2O_4$ composite's elements ($CoFe_2O_4$ and polypyrrole) are non-toxic and stable throughout a wide pH range, making it environmentally friendly and sustainable for practical operations.

Conclusions

The present investigation reveals that the PPy/$CoFe_2O_4$ nanocomposite functions as a proficient adsorbent for the extraction of Pb(II)

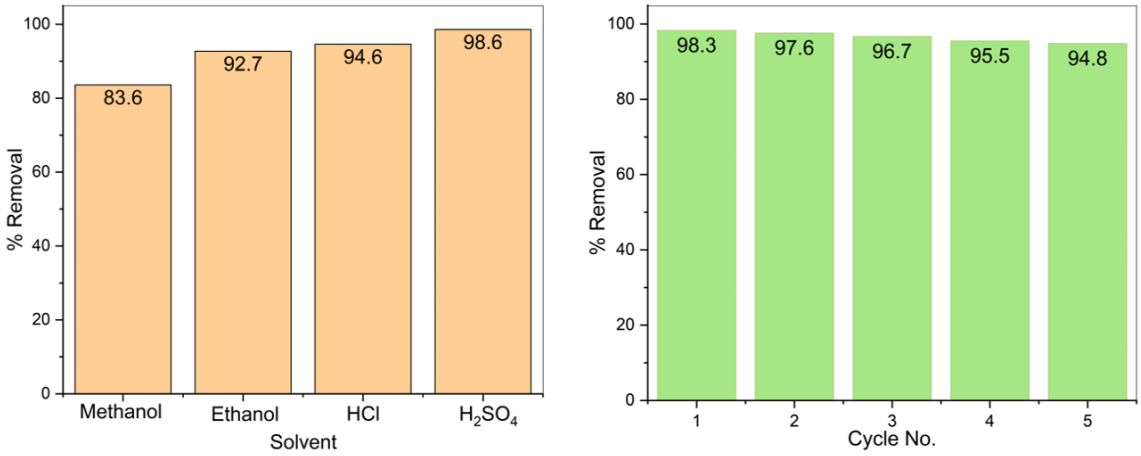

Fig. 9 (a) Effect of solvent on regeneration of PPy/$CoFe_2O_4$. (b) PPy/$CoFe_2O_4$ reusability.

from water-based solutions. The factors that significantly influenced the adsorption process include the starting concentration of Pb(II), the dose of PPy/$CoFe_2O_4$ applied, the contact duration between adsorbate and adsorbent, as well as the pH level of the solution. The optimum pH value for Pb(II) adsorption has been established at 8.0. The PPy/CoFe2O4 composite demonstrated remarkable efficacy in the Pb(II) adsorption, showcasing its potential for effective removal strategies. The examination of isotherms demonstrated that the Langmuir model provided the most precise representation of the equilibrium results for Pb(II) removal, showcasing an ultimate monolayer adsorption capacity of 357.14 mg·g^{-1}. With the equilibrium phase reached within 70 min, it has been demonstrated that a Pb(II) adsorption process could potentially be described by a pseudo-second-order kinetic model. The most effective desorption of Pb(II) from PPy/$CoFe_2O_4$ was accomplished with 0.2 M H_2SO_4, and for five adsorption/desorption cycles, the magnetic PPy/$CoFe_2O_4$ can be effectively reused. In summary, PPy/$CoFe_2O_4$ serves as a highly efficient magnetic nano sorbent, distinguished by its remarkable reusability and ease of magnetic separation, showcasing considerable promise for the extraction of heavy metal ions from wastewater.

Author contributions

The authors confirm contribution to the paper as follows: supervision, conceptualization, statistical analysis: Srivastava A; methodology, investigation, experimental, graphical work: Srivastava N; investigation, formal analysis: Nayak R, Singh R; writing original draft: Srivastava A, Nayak R, Singh R. All authors reviewed the results and approved the final version of the manuscript.

Data availability

The supporting datasets generated during and/or analyzed during the current study are available from the corresponding author on reasonable request.

Acknowledgments

This research project was funded by the Council of Science and Technology, U.P. (Project ID 2093) awarded to Abhishek Srivastava. The authors are thankful to the CST UP for providing financial support.

Conflict of interest

The authors declare that they have no conflict of interest.

Dates

Received 6 December 2024; Revised 18 February 2025; Accepted 24 February 2025; Published online 2 April 2025

References

1. Tundwal A, Kumar H, Binoj BJ, Sharma R, Kumari R, et al. 2024. Conducting polymers and carbon nanotubes in the field of environmental remediation: Sustainable developments. *Coordination Chemistry Reviews* 500:215533
2. Goswami MK, Srivastava A, Dohare RK, Tiwari AK, Srivastav A. 2023. Recent advances in conducting polymer-based magnetic nanosorbents for dyes and heavy metal removal: fabrication, applications, and perspective. *Environmental Science and Pollution Research* 30:73031–60
3. Sable H, Singh V, Kumar V, Roy A, Pandit S, et al. 2024. Toxicological and bioremediation profiling of nonessential heavy metals (mercury, chromium, cadmium, aluminium) and their impact on human health: A review. *Toxicologie Analytique et Clinique* 36:205–34
4. Afzal A, Mahreen N. 2024. Emerging insights into the impacts of heavy metals exposure on health, reproductive and productive performance of livestock. *Frontiers in Pharmacology* 15:1375137
5. Jadaa W, Mohammed H. 2023. Heavy metals–definition, natural and anthropogenic sources of releasing into ecosystems, toxicity, and removal methods–an overview study. *Journal of Ecological Engineering* 24:249–71
6. Fulke AB, Ratanpal S, Sonker S. 2024. Understanding heavy metal toxicity: Implications on human health, marine ecosystems and bioremediation strategies. *Marine Pollution Bulletin* 206:116707
7. Nriagu J. 2023. Sixty years since the report of global lead pollution. *Nature* 619:704–6
8. Huang H, Guan H, Tian ZQ, Chen MM, Tian KK, et al. 2024. Exposure sources, intake pathways and accumulation of lead in human blood. *Soil Security* 15:100150
9. Moyebi OD, Lebbie T, Carpenter DO. 2024. Standards for levels of lead in soil and dust around the world. *Reviews on Environmental Health*. https://doi.org/10.1515/reveh-2024-0030
10. Raj K, Das AP. 2023. Lead pollution: Impact on environment and human health and approach for a sustainable solution. *Environmental Chemistry and Ecotoxicology* 5:79–85
11. Sample L. 2024. Lead Exposure in Children: Failure to Protect the Most Vulnerable. *The Journal of Pediatric Pharmacology and Therapeutics* 29:212–14
12. Ratageri VH. 2025. Lead exposure: the silent threat stifling future generations. *Indian Journal of Pediatric* 92:112–13
13. Sahu MC, Yogeshbhai MR, Oza H, Upadhyay K, Chanania K, et al. 2024. Blood lead levels in pregnant women and their newborn infants at an Indian teaching hospital. *Journal of Family Medicine and Primary Care* 13:348–55
14. Kinuthia GK, Ngure V, Beti D, Lugalia R, Wangila A, et al. 2020. Levels of heavy metals in wastewater and soil samples from open drainage channels in Nairobi, Kenya: community health implication. *Scientific Reports* 10:8434
15. Ayach J, El Malti W, Duma L, Lalevée J, Al Ajami M, et al. 2024. Comparing conventional and advanced approaches for heavy metal removal in wastewater treatment: an in-depth review emphasizing filter-based strategies. *Polymers* 16:1959
16. Jasim AQ, Ajjam SK. 2024. Removal of heavy metal ions from wastewater using ion exchange resin in a batch process with kinetic isotherm. *South African Journal of Chemical Engineering* 49:43–54
17. Villena-Martínez EM, Alvizuri-Tintaya PA, Lora-García J, Torregrosa-López JI, Lo-Iacono-Ferreira VJ. 2022. Reverse osmosis modeling study of lead and arsenic removal from drinking water in Tarija and La Paz, Bolivia. *Processes* 10:1889
18. Hama Aziz KH, Mustafa FS. 2024. Advanced oxidation processes for the decontamination of heavy metal complexes in aquatic systems: A review. *Case Studies in Chemical and Environmental Engineering* 9:100567
19. Deb A, Das S, Debnath A. 2023. Fabrication and characterization of organometallic nanocomposite for efficient abatement of dye laden wastewater: CCD optimization, adsorption mechanism, co-existing ions, and cost analysis. *Chemical Physics Letters* 830:140820
20. Benalia A, Atime L, Baatache O, Khalfaoui A, Ghomrani AF, et al. 2024. Removal of lead in water by coagulation flocculation process using Cactus-based natural coagulant: optimization and modeling by response surface methodology (RSM). *Environmental Monitoring and Assessment* 196:244
21. Ratan S, Srivastava A, Gangwar C, Nayak R, Pandey V, et al. 2024. Adsorption of Pb(II) on Modified Ground Nut Shell (MGNS): Isotherm, kinetic, and thermodynamic study. *Indian Journal of Engineering and Materials Sciences* 31:425–33
22. Shakir HA, Ali Alsaffar M, Mageed AK, Sukkar KA, Abdel Ghany MA. 2024. Optimizing photocatalytic lead removal from wastewater using ZnO/ZrO_2: a response surface methodology approach. *ChemEngineering* 8:72
23. Castro K, Abejón R. 2024. Removal of heavy metals from wastewaters and other aqueous streams by pressure-driven membrane technologies: an outlook on reverse osmosis, nanofiltration, ultrafiltration and microfiltration potential from a bibliometric analysis. *Membranes* 14:180

24. Das S, Pal A, Debnath DA. 2023. Polyaniline-coated magnesium ferrite nanocomposite: synthesis, characterization, fabrication cost analysis and dye sorption behavior with scale-up design. *Chemistry Select* 8:e202300928
25. Ghahremani A, Manteghian M, Kazemzadeh H. 2021. Removing lead from aqueous solution by activated carbon nanoparticle impregnated on lightweight expanded clay aggregate. *Journal of Environmental Chemical Engineering* 9:104478
26. Pyrzynska K. 2023. Recent applications of carbon nanotubes for separation and enrichment of lead ion. *Separations* 10:152
27. Wang H, Wang S, Wang S, Fu L, Zhang L. 2023. Efficient metal-organic framework adsorbents for removal of harmful heavy metal Pb(II) from solution: Activation energy and interaction mechanism. *Journal of Environmental Chemical Engineering* 11:109335
28. Birniwa AH, Kehili S, Ali M, Musa H, Ali U, et al. 2022. Polymer-based nano-adsorbent for the removal of lead ions: kinetics studies and optimization by response surface methodology. *Separations* 9:356
29. Juturu R, Selvaraj R, Murty VR. 2024. Efficient removal of hexavalent chromium from wastewater using a novel magnetic biochar composite adsorbent. *Journal of Water Process Engineering* 66:105908
30. Houshiar M, Zebhi F, Razi ZJ, Alidoust A, Askari Z. 2014. Synthesis of cobalt ferrite ($CoFe_2O_4$) nanoparticles using combustion, coprecipitation, and precipitation methods: A comparison study of size, structural, and magnetic properties. *Journal of Magnetism and Magnetic Materials* 371:43–48
31. Kumar Y, Pramanik P, Das DK. 2019. Electrochemical detection of paracetamol and dopamine molecules using nano-particles of cobalt ferrite and manganese ferrite modified with graphite. *Heliyon* 5:e02031
32. Wang W, Ren J, Wang C, Zheng M, Ma Y, et al. 2022. Magnetic Fe_3O_4/polypyrrole-salicylaldehyde composite for efficient removal of Mn (VII) from aqueous solution by double-layer adsorption. *Journal of Applied Polymer Science* 139:e52515
33. Patra C, Shahnaz T, Subbiah S, Narayanasamy S. 2020. Comparative assessment of raw and acid-activated preparations of novel Pongamia pinnata shells for adsorption of hexavalent chromium from simulated wastewater. *Environmental Science and Pollution Research* 27:14836–51
34. Valsalakumar VC, Sreevalli Y, Archana PK, Joseph AS, Ubaid S, et al. 2024. Removal of anionic dye from textile effluent using zirconium phosphate loaded polyaniline-graphene oxide composite: lab to pilot scale evaluation. *Journal of Environmental Management* 368:122068
35. Soltani-Nezhad S, Mashreghi A, Hasani S, Rezvan MT, Ziarati A. 2024. Application of Taguchi method to optimize the properties of cobalt ferrite nanoparticles doped by Ca^{2+} and Gd^{3+}. *Inorganic Chemistry Communications* 159:111759
36. Pourgolmohammad B, Masoudpanah SM, Aboutalebi MR. 2017. Synthesis of $CoFe_2O_4$ powders with high surface area by solution combustion method: Effect of fuel content and cobalt precursor. *Ceramics International* 43:3797–803
37. Ren J, Wang C, Zhang H, Liu X, Yan T, et al. 2023. Magnetic Core@Shell Fe_3O_4@Polypyrrole@Sodium dodecyl sulfate composite for enhanced selective removal of dyestuffs and heavy metal ions from complex wastewater. *Langmuir* 39:10098–11
38. Shyamaldas, Bououdina M, Manoharan C. 2020. Dependence of structure/morphology on electrical/magnetic properties of hydrothermally synthesised cobalt ferrite nanoparticles. *Journal of Magnetism and Magnetic Materials* 493:165703
39. Hair ML. 1980. Transmission infrared spectroscopy for high surface area oxides. In *Vibrational Spectroscopies for Adsorbed Species*. Washington, D.C., US: American Chemical Society. pp. 1–11. doi: 10.1021/bk-1980-0137.ch001
40. Aziz C, Azhdar B. 2022. Synthesis of dysprosium doped cobalt ferrites nanoparticles by solgel auto-combustion method and influence of grinding techniques on structural, Morphological, and magnetic properties. *Journal of Magnetism and Magnetic Materials* 542:168577
41. Hussain D, Siddiqui MF, Shirazi Z, Khan TA. 2022. Evaluation of adsorptive and photocatalytic degradation properties of $FeWO_4$/polypyrrole nanocomposite for rose bengal and alizarin red S from liquid phase: Modeling of adsorption isotherms and kinetics data. *Environmental Progress and Sustainable Energy* 41:e13822
42. Yuan L, Wan C, Ye X, Wu F. 2016. Facial synthesis of silver-incorporated conductive polypyrrole submicron spheres for supercapacitors. *Electrochimica Acta* 213:115–23
43. Ali H, Ismail AM. 2023. Fabrication of Magnetic Fe_3O_4/Polypyrrole/Carbon Black Nanocomposite for Effective Uptake of Congo Red and Methylene Blue Dye: Adsorption Investigation and Mechanism. *Journal of Polymers and the Environment* 31:976–998
44. Taha AA, Kandil S, Mohamed LA, Sallam MG, Heiba HF. 2023. Surface investigations of selective biosorption and reduction of hexavalent chromium ions Cr(VI) over chitosan@MoO_3 and chitosan-cellulose@MoO_3 biocomposite. *Journal of Molecular Structure* 1288:135716
45. Sadeghi MM, Rad AS, Ardjmand M, Mirabi A. 2018. Preparation of magnetic nanocomposite based on polyaniline/Fe_3O_4 towards removal of lead (II) ions from real samples. *Synthetic Metals* 245:1–9
46. Arabahmadi V, Ghorbani M. 2017. Pb(II) removal from water using surface modified polythiophene coated rice husk ash nanocomposite. *Inorganic and Nano-Metal Chemistry* 47:1614–24
47. Masoud MS, Haggag SS, Heiba HF, Abd El-Hamed OH, Habila NS, et al. 2023. Comparative adsorption affinities of nano-metal oxides towards Cr(VI): synthesis, characterization, kinetics, isotherms, thermodynamic and techno-economics study. *Environmental Processes* 10:33
48. Bushra R, Naushad M, Adnan R, ALOthman ZA, Rafatullah M. 2015. Polyaniline supported nanocomposite cation exchanger: Synthesis, characterization and applications for the efficient removal of Pb^{2+} ion from aqueous medium. *Journal of Industrial and Engineering Chemistry* 21:1112–18
49. Budhiraja T, Rawat V, Kimothi S, Dumka UC, Gupta R, et al. 2024. Low temperature physical activation of raw charcoal for excellent dye adsorption kinetics. *Fullerenes Nanotubes and Carbon Nanostructures* 33:441–55
50. Ghasemi M, Naushad M, Ghasemi N, Khosravi-fard Y. 2014. A novel agricultural waste based adsorbent for the removal of Pb(II) from aqueous solution: Kinetics, equilibrium and thermodynamic studies. *Journal of Industrial and Engineering Chemistry* 20:454–61
51. Chen K, He J, Li Y, Cai X, Zhang K, et al. 2017. Removal of cadmium and lead ions from water by sulfonated magnetic nanoparticle adsorbents. *Journal of Colloid and Interface Science* 494:307–16
52. Rafiei HR, Shirvani M, Ogunseitan OA. 2016. Removal of lead from aqueous solutions by a poly(acrylic acid)/bentonite nanocomposite. *Applied Water Science* 6:331–38
53. Tan Y, Chen M, Hao Y. 2012. High efficient removal of Pb (II) by amino-functionalized Fe_3O_4 magnetic nano-particles. *Chemical Engineering Journal* 191:104–11
54. Naushad M, ALOthman ZA, Awual MR, Alam MM, Eldesoky GE. 2015. Adsorption kinetics, isotherms, and thermodynamic studies for the adsorption of Pb^{2+} and Hg^{2+} metal ions from aqueous medium using Ti(IV) iodovanadate cation exchanger. *Ionics* 21:2237–45
55. Rusmin R, Sarkar B, Tsuzuki T, Kawashima N, Naidu R. 2017. Removal of lead from aqueous solution using superparamagnetic palygorskite nanocomposite: material characterization and regeneration studies. *Chemosphere* 186:1006–15
56. Çelik MS, Çaylak O, Kütük N, Yenidünya AF, Çetinkaya S, et al. 2025. Removal of lead ions (Pb^{2+}) from aqueous solution using chitosan/starch composite material: experimental and density functional theory findings. *Biomass Conversion and Biorefinery* 15:1041–56
57. Weber TW, Chakravorti RK. 1974. Pore and solid diffusion models for fixed bed adsorbers. *American Institute of Chemical Engineers* 20:228–38
58. Freundlich H. 1906. Über die Adsorption in Lösungen [Over the Adsorption in Solution]. *Zeitschrift für Physikalische Chemie [Physical Chemistry and Chemical Physics]* 57:385–470